

Spatial correlations and dispersion for fluid transport through packed glass beads studied by pulsed field-gradient NMR

S. Stapf,^{1,*} K. J. Packer,¹ R. G. Graham,¹ J.-F. Thovert,² and P. M. Adler³

¹*Department of Chemistry, University of Nottingham, Nottingham NG7 2RD, United Kingdom*

²*Laboratoire des Phénomènes de Transport dans les Mélanges (LPTM), 86960 Futuroscope Cedex, France*

³*Institut de Physique du Globe de Paris (IPGP), Tour 24, 4 Place Jussieu, 75252 Paris Cedex 05, France*

(Received 31 March 1998)

The two-dimensional displacement joint probability density $P_{\Delta}(X,Z)$ for water flowing through a bed of glass beads has been measured by means of pulsed field-gradient nuclear magnetic resonance. The simultaneous particle displacements X and Z perpendicular and parallel to the pressure gradient, respectively, at a given encoding time Δ , are obtained from an experiment employing orthogonal magnetic field gradients. The resulting probability density distribution is compared to numerical simulations of flow through an equivalent system of randomly deposited monodisperse spheres. The dependence of the centered second moments in X and Z on flow time is discussed for the experimental and simulated data. A crossover from a time scale dominated by Brownian motion toward a behavior determined by the convective flow and velocity fluctuations is observed. The mutual dependence between displacements perpendicular and parallel to the flow direction is revealed in the evolution of a correlation coefficient $\rho_{X^2,Z}$. This coefficient is found to increase for short times and to decrease for larger displacements, with a maximum at an average displacement corresponding to the bead radius. As a means of displaying the cause of these correlations, a correlation probability density $C_{\Delta}(X,Z) = P_{\Delta}(X,Z) - P_{\Delta}(X)P_{\Delta}(Z)$ is suggested, where $P_{\Delta}(X)$ and $P_{\Delta}(Z)$ are the marginals of $P_{\Delta}(X,Z)$. A plot of this matrix renders zero in the absence of correlations, but produces a characteristic pattern of positive and negative regions when displacements in X are correlated with those in Z . The time evolution of this pattern is discussed and compared to the shape of model propagators obtained from an analytical function and a numerical simulation for a simplified capillary array, respectively. [S1063-651X(98)05611-6]

PACS number(s): 47.55.Mh, 81.05.Rm, 47.11.+j, 83.70.Gp

I. INTRODUCTION

Transport and dispersion of fluid phases and solutes within porous solid structures is of importance in a wide range of areas such as oil reservoir appraisal and management, aquifer behavior, distillation and filtration processes, heterogeneous catalyst bed design and performance, pollutant dispersal and recovery in the environment, etc. The field has an extensive literature, and a wide range of experiments have been performed, many of which have been summarized in three major references [1–3], with historically important compilations and data being also found in Refs. [4,5]. Few theoretical results are available to describe these fluid transport processes, except for the case of Poiseuille flow [6,7] and for dilute suspensions [8]. Numerical results for long time behavior have been obtained for two- [9,10] and three-dimensional [11] structures. Some consideration has been given to the early time dispersion behavior of solutes, the so-called non-Fickian or nonlocal regime, both experimentally [12,13] and theoretically [14,15]. In the latter approach, the convection-diffusion equation was solved symbolically in terms of a Green function P , which gives the probability of finding a tracer at position \mathbf{r} at time t , given that it was

known to be at \mathbf{r}_0 at t_0 . This Green function was used to express the average mass flux as a function of the initial concentration distribution, with the resulting expression being rearranged and a time-dependent dispersion tensor introduced, which generalizes the classical local dispersion. So far, this has been worked out only for fluid transport through a dilute suspension of spheres, although it was claimed that it could be extended to larger solid phase volume fractions. Experimental data from closely packed beds of spheres [13] have shown only modest and qualitative agreement with this theory.

Of the many experimental approaches to the characterization of fluid transport in porous solids, nuclear magnetic resonance (NMR) has a number of significant advantages. Principal among these is the fact that NMR studies the fluid directly and is able to investigate optically opaque systems, which constitute the majority of those of interest. A particularly powerful NMR method is that based on the use of magnetic field-gradient pulses to determine the statistics of nuclear spin (and, hence, molecular) displacements [16]. Such pulsed gradient spin echo (PGSE) NMR methods are based on the propagator formalism [17] which directly gives $P_{\Delta}(\mathbf{R})$, the probability distribution of displacements $\mathbf{R} = \mathbf{r}(\Delta) - \mathbf{r}(0)$ in time Δ . This method has been used experimentally to characterize the diffusive-convective transport through a number of model porous solids [18–25]. The availability of increased computational power has made possible simulations with sufficient spatial and temporal resolu-

*Author to whom correspondence should be addressed. FAX: +44-115-951-3562.

Electronic address: pczssx@unix.ccc.nottingham.ac.uk

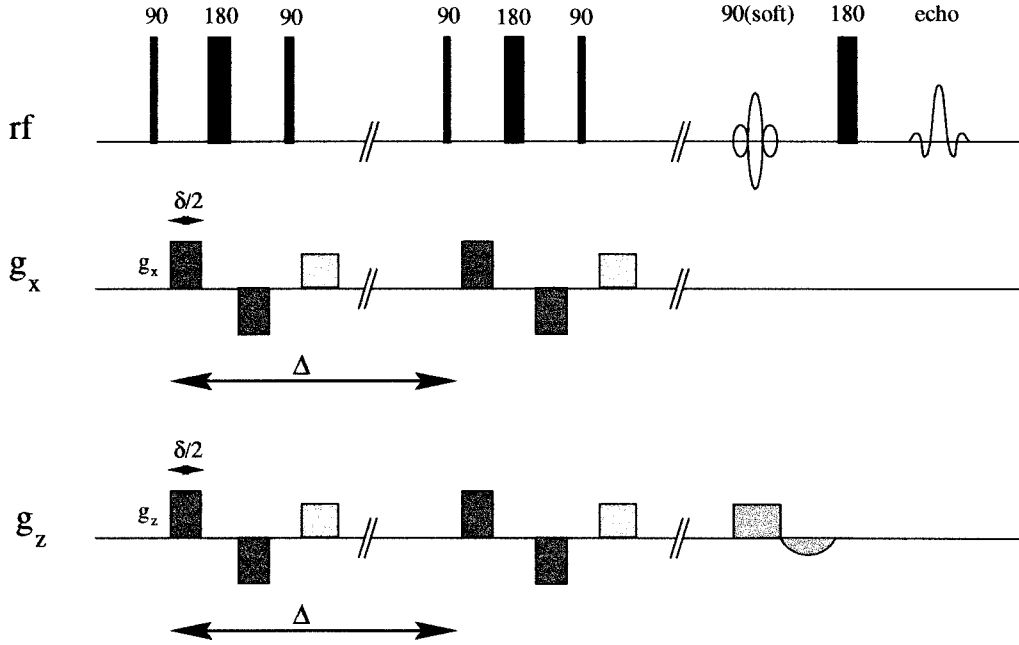


FIG. 1. Pulse sequence used for measuring two-dimensional average propagators. rf hard pulses are given by black rectangles, and the slice selective pulse is indicated by its sinc shape. Gradient pulses in dark gray are encoding gradients, and crusher gradients to remove residual phase coherences are drawn in light gray. The encoding gradients are applied simultaneously in orthogonal directions.

tion to compare directly with experiment [23–25], making use of algorithms which generate realizations of statistical porous systems [11,26]. All measurements reported to date have determined $P_{\Delta}(\mathbf{R})$ for \mathbf{R} either parallel or transverse to the pressure gradient driving the net flow.

However, to our knowledge, no attempt has yet been made to correlate displacements parallel (Z) and perpendicular (X) to the pressure gradient quantitatively with each other for flow in a porous system, either by experimental or computational methods. Preliminary results on flow through a porous sandstone were presented in Ref. [27]. In this paper we determine, by PGSE NMR, the two-dimensional joint probability density $P_{\Delta}(X,Z)$ for water flow in a bed of randomly deposited glass beads. The time evolution of this propagator, as well as that of the moments and correlation coefficients connected to X and Z , are described and compared with extensive computer simulations.

II. THEORY

To obtain the two-dimensional propagator, we have modified the alternating pulsed field-gradient stimulated echo (APGSTE) version [28] of the PGSTE sequence [29]. In addition to the original sequence, a second set of gradient pulses has been added; gradients in both orthogonal directions are switched simultaneously (see Fig. 1).

The splitting of the defocussing and refocussing gradients by insertion of a rf pulse of flip angle π minimizes the effect of molecular displacements through the internal magnetic field gradients, which arise from the differences of magnetic susceptibility existing between the porous solid matrix and the saturating fluid [30]. As described in Ref. [28], offsetting the phase of the second $\pi/2$ pulse by 90° allows discrimination between positive and negative displacements.

Each nuclear spin i experiences a phase shift ϕ_i that is

proportional to its position at time 0 and to the area of the gradient,

$$\phi_i(\mathbf{g}, \delta, \mathbf{r}_i(0)) = \delta\omega(\mathbf{r}_i(0)) = \delta\{\gamma B_0 + \gamma \mathbf{g} \cdot \mathbf{r}_i(0)\}, \quad (1)$$

where $|\mathbf{g}|$ and δ are the strength and duration of the applied gradient, respectively, γ is the gyromagnetic ratio, and B_0 denotes the static magnetic field. $\omega(\mathbf{r}_i)$ is the Larmor frequency at the position \mathbf{r}_i . After an evolution time Δ , the refocusing gradient results in a negative phase shift which leaves the resultant shift

$$\phi_i(\Delta) = \gamma \delta \mathbf{g} \cdot \{\mathbf{r}_i(\Delta) - \mathbf{r}_i(0)\} = \gamma \delta \mathbf{g} \cdot \mathbf{R}_i(\Delta), \quad (2)$$

where $\mathbf{R}_i(\Delta) = \mathbf{r}_i(\Delta) - \mathbf{r}_i(0)$ indicates the displacement for particle i during the observation time Δ . The total signal amplitude is obtained by summation over all spins, equivalent to the integral

$$S_{\Delta}(\mathbf{q}) = \int P_{\Delta}(\mathbf{R}) \exp\{i2\pi \mathbf{q} \cdot \mathbf{R}(\Delta)\} d\mathbf{R}, \quad (3)$$

where $\mathbf{q} = (2\pi)^{-1} \gamma \delta \mathbf{g}$, and the average propagator $P_{\Delta}(\mathbf{R}) = \int P(\mathbf{r}_0) P(\mathbf{r}, \Delta; \mathbf{r}_0) d\mathbf{r}_0$. $P(\mathbf{r}_0)$ is the probability density for starting positions, while $P(\mathbf{r}, \Delta; \mathbf{r}_0)$ is the conditional probability for displacements from \mathbf{r}_0 to \mathbf{r} in time Δ , equivalent to the Green function mentioned above [14,15].

The average propagator $P_{\Delta}(\mathbf{R})$ can therefore be obtained directly by Fourier transformation of $S_{\Delta}(\mathbf{q})$ with respect to \mathbf{q} . Under the circumstances of this study, \mathbf{q} consists of two orthogonal components q_z and q_x ; thus

$$\mathbf{q} = \mathbf{k}q_z + \mathbf{i}q_x, \quad (4)$$

where \mathbf{k} and \mathbf{i} are unit vectors along z and x , respectively. z is parallel to the pressure gradient driving the fluid flow, and

x is perpendicular to it. The two-dimensional average propagator $P_{\Delta}(X,Z)$, for displacements X and Z , is then calculated by successive fast-Fourier transform in both directions. It must be mentioned that Eq. (3) is only applicable if the duration of the gradient pulse is negligible compared to the experimental time ($\delta \ll \Delta$).

The boundary conditions imposed experimentally (see below) ensure that there is no net radial flow and the system is therefore axially symmetric. The propagator for displacements in the x -direction, $P_{\Delta}(X)$, is therefore identical for all directions perpendicular to the flow axis.

III. EXPERIMENT

The NMR measurements were carried out using a GEΩ CSI spectrometer operating for proton resonance at 85 MHz, the field being provided by an Oxford Instruments 85/310 horizontal bore magnet equipped with room temperature shims and S-150 Accustar actively shielded gradient coils providing gradients of up to 0.2 T m^{-1} . Phase cycling of the rf pulses [28] was used to minimize the effects of background gradients and dc offsets.

A sample of glass beads of $600 \pm 50\text{-}\mu\text{m}$ diameter [Jencons (Scientific) Ltd., Leighton Buzzard, UK, Cat. No. H102/1/126] was prepared by filling a glass tube of 27.2-mm inner diameter and 120-mm length with water and adding the wet glass beads and water suspension slowly, allowing the beads to sediment. Air bubbles were removed by stirring during the filling process. The tube was fitted at both ends with sintered glass disks to ensure an even distribution of streamlines over the whole cross-section. The sample was connected, via a 2-m narrow-bore pipe, to a precision pump (Pharmacia P50) which was operated at constant volume flow rates of 4.8, 14.0, and 42.0 ml/min, respectively. The relaxation time of the flowing water was reduced to $T_1 = 600 \text{ ms}$ by adding copper(II) sulfate, allowing a pulse sequence repetition time of 3.3 s.

Experiments were performed using the APGSTE pulse sequence given in Fig. 1. The signal was acquired using a slice-selective soft pulse with an effective axial slice thickness of 60 mm located symmetrically at the center of the sample. This was used in order to avoid edge effects which could arise from the inflow and outflow of water at the ends of the sample. Two-dimensional data sets were obtained by stepwise variation of the strength of the pulsed gradients simultaneously applied parallel and perpendicular to the flow direction. Data were acquired using $n_x - 2$ and $n_z - 2$ evenly spaced positive and two negative gradient values, respectively, where n_x and n_z denote the total dimensionality in X and Z directions, and were chosen as powers of 2 (typically $n_x = 16$, $n_z = 32$ or 64). Measurements at the two negative gradient values served to determine the zero- q phase shift which enabled the reconstruction of the full data set of dimension $(2n_x - 4) \times (2n_z - 4)$. This matrix was then Fourier transformed numerically after zero filling to twice the original size, and subsequently phase corrected. The marginals $P_{\Delta}(X)$ and $P_{\Delta}(Z)$ of the resulting propagator $P_{\Delta}(X,Z)$, defined as

$$P_{\Delta}(X) = \int P_{\Delta}(X,Z) dZ, \quad P_{\Delta}(Z) = \int P_{\Delta}(X,Z) dX, \quad (5)$$

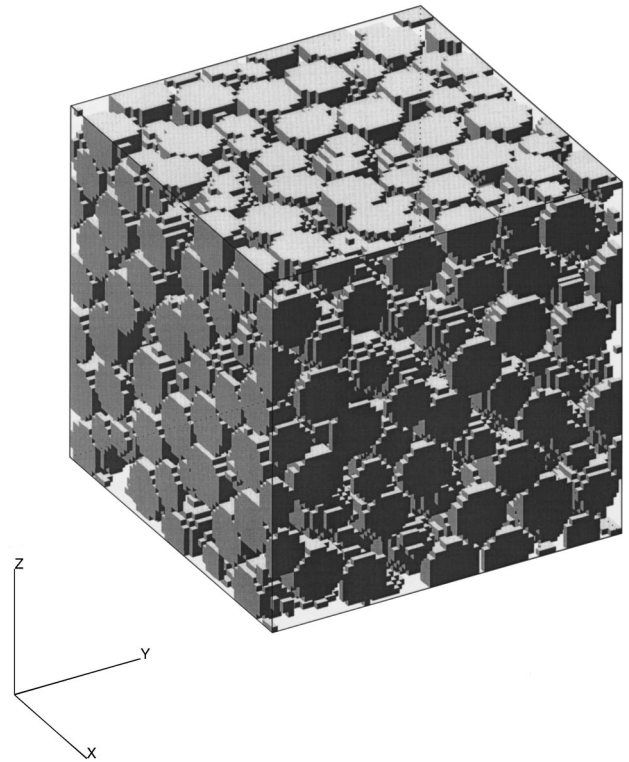


FIG. 2. Example of a reconstructed packed bed of monodisperse spheres.

were compared to one-dimensional propagators obtained under identical conditions but with a higher resolution of 64 or 128 points and with symmetrical gradient steps covering the range $-q_{\max}, \dots, q_{\max}$. The propagators matched satisfactorily. All calculations were performed using interactive data language (IDL) [31].

IV. SIMULATIONS

To generate an adequate representation of the real porous medium, random sphere packing has been simulated by successive deposition of grains in a ‘‘gravitational’’ field. The N th grain is introduced at a random location above the bed of $N - 1$ grains already deposited, and is allowed to fall until it reaches a local minimum of its potential energy. A more detailed description of the deposition process is found in Refs. [26] and [24]. A random packing of monodisperse spheres was generated by this algorithm, incorporating periodic boundary conditions along the two horizontal axes (see Fig. 2). The sample is made of N_C^3 elementary cubes of side $a = 60 \mu\text{m}$, corresponding to $\frac{1}{10}$ of the bead diameter, with $N_C = 64$. The porosity ϵ of the void space was chosen to be $\epsilon = 0.44$. The bed permeability K was calculated by solving the Stokes equations, and was found to be $K = 7140$ Darcy.

In the next step, the velocity field was generated by solving the Stokes equations

$$\nabla p = \mu \nabla^2 \mathbf{v}, \quad \nabla \cdot \mathbf{v} = 0, \quad (6)$$

where \mathbf{v} , p , and μ are the velocity, pressure, and viscosity of the fluid, respectively, and $\mathbf{v} = \mathbf{0}$ on the surface of the wetted solid. The symmetric permeability tensor \mathbf{K} only depends on

the geometry of the system, and describes the relation between the macroscopic pressure gradient $\overline{\nabla p}$ and the seepage velocity $\overline{\mathbf{v}}$:

$$\overline{\mathbf{v}} = -\frac{1}{\mu} \mathbf{K} \overline{\nabla p}. \quad (7)$$

The numerical method used to solve these equations is outlined in Ref. [32]. It assumes low Reynolds numbers which are guaranteed by the experimental conditions employed in this study.

The determination of the average propagator is performed by inserting a large number of particles uniformly distributed within the pore space. For each elementary time step, the particle's position is calculated by adding convective and random diffusive displacements, where the geometrical restrictions of the solid matrix are taken into account. The relative weight of these contributions to the displacement is expressed by the Peclet number

$$\text{Pe} = \frac{\overline{v^*} L}{D}, \quad (8)$$

where $\overline{v^*}$ is the interstitial velocity and L is a characteristic length, taken as being equal to the sphere diameter. The random component is adjusted for a given Peclet number to be as large as possible in order to speed up the statistical convergence, provided that the total elementary jump length is kept smaller than $a/2$ [24]. The precision of these calculations was carefully studied in Ref. [11]; it was concluded that the calculations were reliable for Peclet numbers smaller than 1000.

Following this procedure, typically 2.5×10^5 particles were distributed randomly in the pore space of the lattice, and were allowed to undergo flow and Brownian motion. The self-diffusion coefficient was chosen as $2.1 \times 10^{-9} \text{ m}^2 \text{ s}^{-1}$, the sphere diameter as $6 \times 10^{-4} \text{ m}$, and the interstitial velocity as 2.85×10^{-4} , 8.33×10^{-4} , and $2.5 \times 10^{-3} \text{ m s}^{-1}$, respectively. The latter values correspond to the flow rates used during the experiments, i.e., 4.8, 14.0, and 42.0 ml/min, respectively. Additional simulations were run with smaller numbers of particles for time scales well above and below the experimentally accessible range, and for which the self-diffusion coefficient was also varied over several orders of magnitude.

This simulation technique for obtaining the displacement distributions of the particles is, in a sense, strictly equivalent to the formalism using the Green function which was developed by Koch and Brady [14,15], since it amounts to the solution of the convection-diffusion equation. For this reason, it was not found necessary to rederive it within the nonlocal formalism of Refs. [14,15].

V. MODELING

In order to gain a more direct physical insight into the relationship between the features observed in the experimentally determined joint propagators $P_{\Delta}(X,Z)$ and the underlying pore space characteristics, we have extended the simple model for flow in a porous solid which we introduced earlier [18]. The model used here consists of 10^4 cylindrical capil-

laries of length l and uniform radius, isotropically distributed in orientation. 500 particles are assigned to the start of each capillary at $t=0$. The velocity vectors are oriented in the direction of the capillary, and have magnitudes taken at random from the usual uniform distribution appropriate to laminar flow within a circular pipe. To represent the axial nature of the system, we make $v_{\max} = V_0 \cos \theta$, where θ is the angle between the capillary and the z axis. Coordinates of each particle are then calculated at various times Δ . The important extension of the model from that in Ref. [18] is that particles which reach the end of their starting capillaries within Δ transfer to the start of another capillary in which they continue their motion. The orientation of this second capillary lies on a cone of half-angle α emanating from the end of the starting capillary. α is constant for each calculation, but is varied in order to give insight into the way in which locally discrete changes in flow direction influence the propagators $P_{\Delta}(X,Z)$. The final results from all 5×10^6 trials for each α are collected in a $64 \times 64 \times 64$ three-dimensional histogram, and stored on disc for further processing. Although the use of such a model may be criticized as being based on a physically unrealistic representation of a real pore space, such models and more sophisticated versions of them are widely used for investigating fluid transport in porous solids [33].

VI. RESULTS AND DISCUSSION

A. Experiments and simulations on spherical beads

To investigate the influence of characteristic system dimensions, both flow rate and encoding time were varied in the experiments over a range of average displacements covering two orders of magnitude from much less than the bead size of $600 \mu\text{m}$ to about 2 mm. The experiments were restricted by the required condition $\Delta/\delta \gg 1$; the smallest ratio used was larger than 8. On the other hand, encoding times exceeding the longitudinal relaxation time T_1 by far were not considered feasible due to the loss of signal intensity. This range, however, could be expanded in the simulations where similar restrictions do not apply.

In addition, the flow rates had to be chosen to result in Peclet and Reynolds numbers Pe and Re to comply with the conditions of the simulations. For the three flow rates used in the experiment (4.8, 14.0, and 42.0 ml/min, respectively), one obtains $\text{Pe} = 88, 245, \text{ and } 720$, where Eq. (8) has been used with $L = 600 \mu\text{m}$. Some simulations were run with higher Peclet numbers but only for short times, where it has been found that the method used is still valid [24]. The Reynolds number is defined as

$$\text{Re} = \frac{\overline{v^*} L}{\nu}, \quad (9)$$

with ν being the kinematic viscosity of the liquid. Re indicates the ratio of inertial and viscous forces, and should not be much larger than unity for optimal simulation results; in this case, it took the three values 0.15, 0.5, and 1.4, respectively. For such low Reynolds numbers, the deviations of the real velocity field from the solution of the Stokes equations are expected to be very small.

Two-dimensional propagators (joint probability densities for displacements X and Z) for water flowing in the column

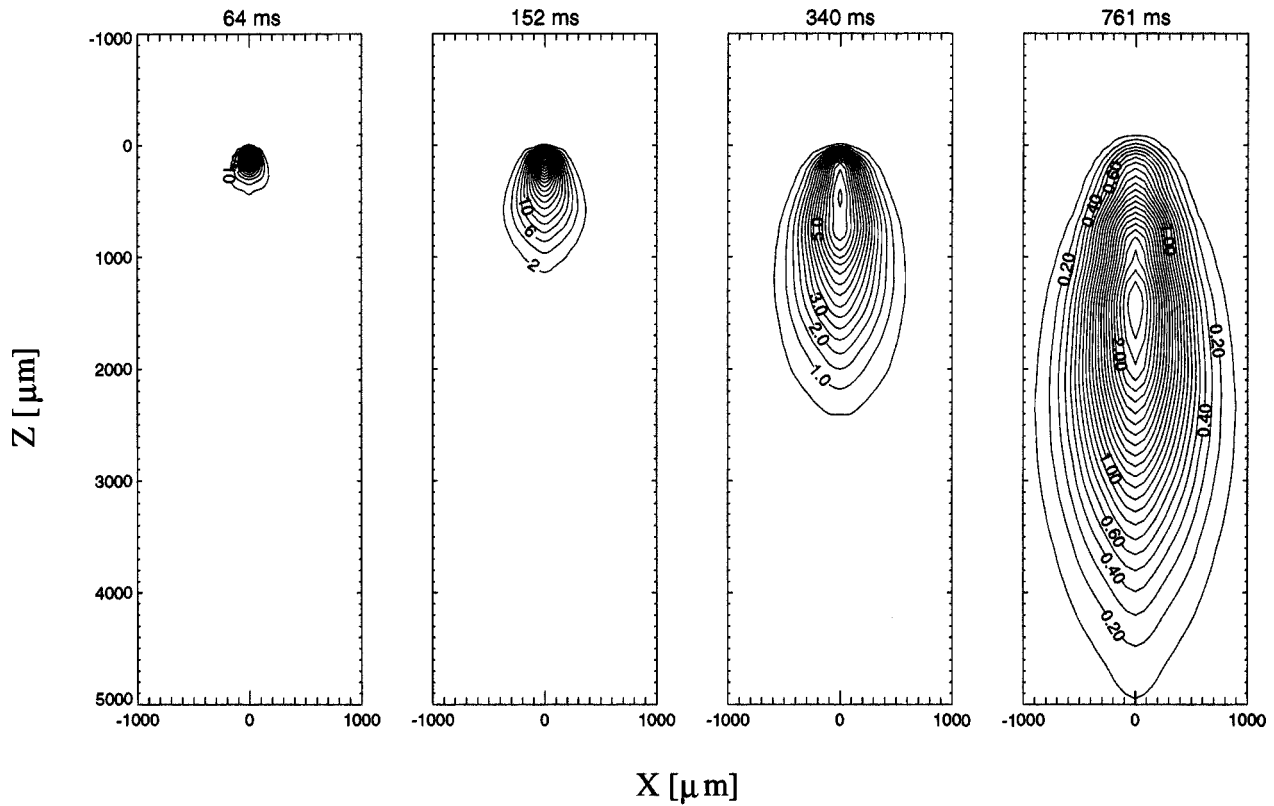


FIG. 3. Two-dimensional average propagator $P_{\Delta}(X,Z)$ for experimental data at a flow rate of 42.0 ml/min. All propagators are normalized to $\iint P_{\Delta}(X,Z)dX dZ=1$. Contour lines are drawn from approximately 0.05 of the peak intensity in linear spacing; numbers indicate probability densities in 10^4 m^{-2} . Evolution times Δ are as indicated.

of packed glass beads are shown in Fig. 3 for the 42.0-ml/min flow rate, and for encoding times between 64 and 761 ms. The contour lines indicate regions of equal probability density. Numbers at each line are given in 10^4 m^{-2} and the propagator is normalized so that $\iint P_{\Delta}(X,Z)dX dZ=1$. The propagator is symmetric in X , which is a consequence of the experimental constraint that no net flow occurs perpendicular to the pressure gradient. In the Z direction, the fraction of particles experiencing negative displacements is very small, while a pronounced peak near zero displacement is found for short times.

It can be seen immediately that the lines of equal probability density spread in both directions with increasing time. At the shortest time $\Delta=64$ ms, when the mean displacement $\langle Z \rangle$ in the flow direction is $160 \mu\text{m}$, considerably less than the bead size, and when the root-mean-square displacement due to diffusion, $\sqrt{\langle Z^2(\Delta) \rangle}$, is only $16 \mu\text{m}$, the total spread at the outermost line (corresponding to about $\frac{1}{20}$ of the peak probability density) is almost the same in X and Z . Thus, for an average displacement less than the bead size, the particles spread to a similar degree in X and Z . The same is observed from experiments with smaller flow rates and hence even smaller average displacements. For longer times and for larger flow rates, however, the shape of the propagator becomes more elongated, and large particle displacements occur preferentially along Z . A closer look at the shape of individual contour lines reveals that the ratio of their main axes, Z/X , is changing, this ratio being larger for contours of higher probability density. This feature suggests that near the higher levels of probability density, which are associated

with small X displacements, particles possess, on average, much larger displacements in the axial direction than perpendicular to it. In contrast, for those particles which have traveled large distances, the difference between X and Z is considerably less pronounced. This deviation from a symmetric shape of the two-dimensional propagator already indicates a connection between X and Z displacements.

Another feature apparent in Fig. 3 is the position of the peak for each flow time Δ . While it remains near zero for shorter times, it becomes shifted toward larger displacements only for times of 340 ms and larger. A similar behavior has been found previously with one-dimensional measurements [18,24]: A narrow Gaussian peak around $Z=0$ develops a shoulder for increasing times and finally disappears for long times; the shoulder, on the other hand, gives rise to another peak that eventually becomes the center of a Gaussian distribution, and is given by the average displacement $\langle Z \rangle = v^* \Delta$. Observing the one-dimensional propagator $P_{\Delta}(Z)$ alone leads to a simplified interpretation of two components, one quasistatic and the other moving with $v > v^*$. This can be seen by comparing the two-dimensional propagator with its marginals (see Fig. 4): in this example for 42-ml/min flow rate and $\Delta=231$ ms, the peak for $P_{\Delta}(X,Z)$ is still at $Z < 200 \mu\text{m}$, while its projection $P_{\Delta}(Z) = \int P_{\Delta}(X,Z)dX$ shows a maximum probability density near $600 \mu\text{m}$. As the marginal represents an average over all X displacements, part of the information about the real properties of the displacement probabilities in two (or three) dimensions is lost, which can lead to misinterpretations.

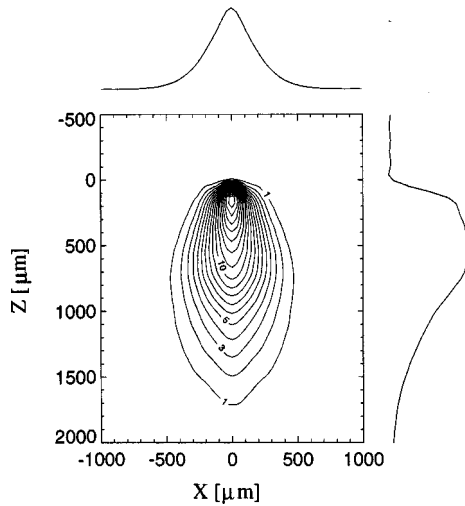


FIG. 4. Two-dimensional average propagator $P_{\Delta}(X,Z)$ for experimental data at a flow rate of 42.0 ml/min, $\Delta=231$ ms. The marginals $P_{\Delta}(X)$ and $P_{\Delta}(Z)$ are drawn along the X and Z axis, respectively.

In Fig. 5, simulated propagators at equivalent times are shown for comparison. A similarity is observed for the general shape of the contour lines and their axis ratios. However, a major difference can be found with respect to the peak of maximum probability density. It is much more persistent in the simulation than in the experiment, being prominent even at the longest evolution time of 750 ms. In the simulations, it eventually disappears for $\Delta \geq 5$ s. Experiments and simula-

tions generally coincide much better for small average displacements, as long as the marginal $P_{\Delta}(Z)$ can be described by a peak near $Z=0$ and an asymmetrically decaying tail at larger displacements [18,24,25]. The difference between experiment and simulations has been discussed previously, as possibly arising as a consequence of the surface relaxivity that tends to remove a fraction of the molecules near the walls in the NMR experiment [25]. Due to the nonslip condition near the wall, this affects mainly spins with small velocities, and might lead to a faster decay of the peak near $Z \approx 0$. However, allowing a loss of particles at the wall did not influence the result in earlier simulations [24].

The influence of large Peclet and Reynolds numbers was also mentioned in Ref. [24]. As in this previous investigation, edge effects can be ruled out as the inner diameter of the tube is equal to 45 bead diameters.

It must be pointed out that the deviations only affect the peak at small displacements, and therefore a fraction of particles that show small net displacements apart from their Brownian motion; this fraction disappears much later in the simulation. However, the behavior for short times is well represented by the simulations, as well as the probability densities for large displacements. The numerical simulations coincide reasonably well with the experimental results once these limitations are considered.

B. Time and displacement dependence of moments of $P_{\Delta}(X,Z)$

In Sec. VI A, we described the evolution of the propagator $P_{\Delta}(X,Z)$ as a function of time Δ in a qualitative way by

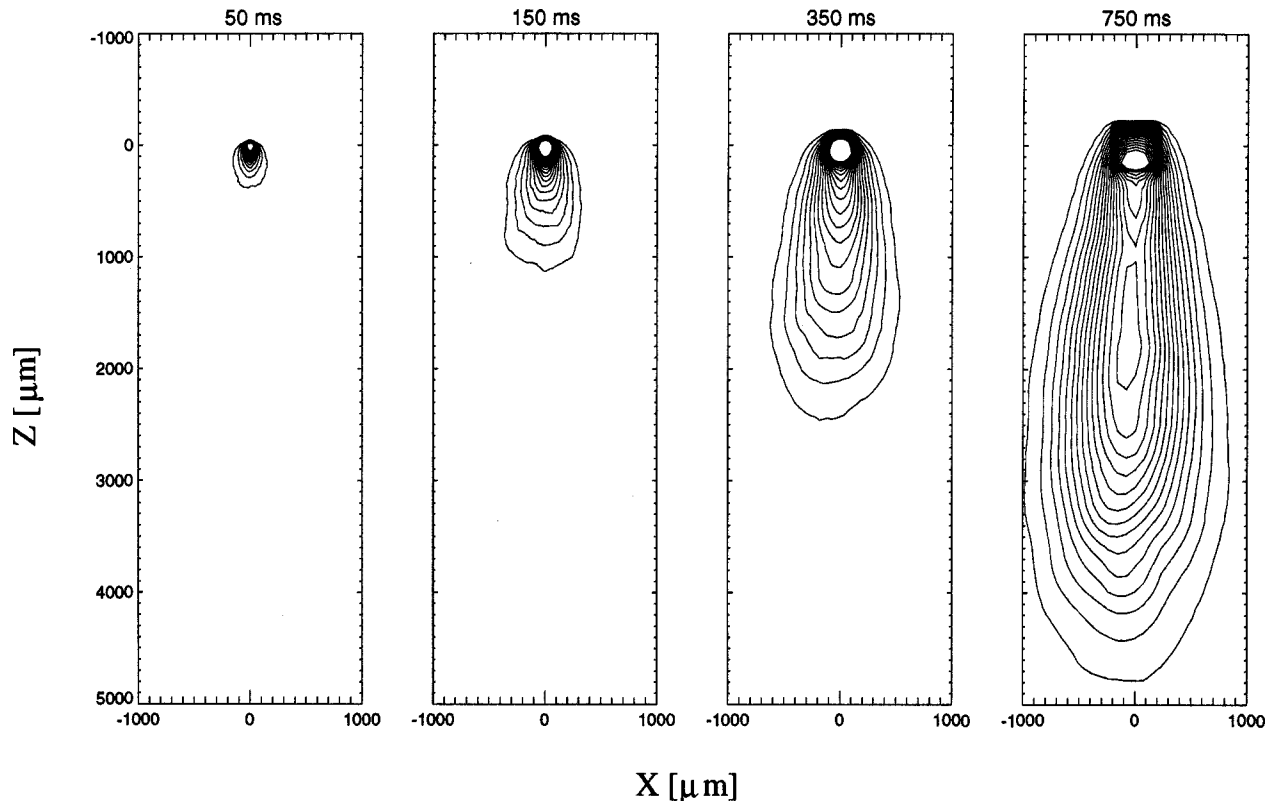


FIG. 5. Two-dimensional average propagator $P_{\Delta}(X,Z)$ for simulated data (250 000 particles) at a flow rate of 42.0 ml/min. All propagators are normalized to $\iint P_{\Delta}(X,Z) dX dZ = 1$. Contour lines are drawn from approximately 0.05 of the peak intensity in linear spacing. Evolution times Δ are as indicated.

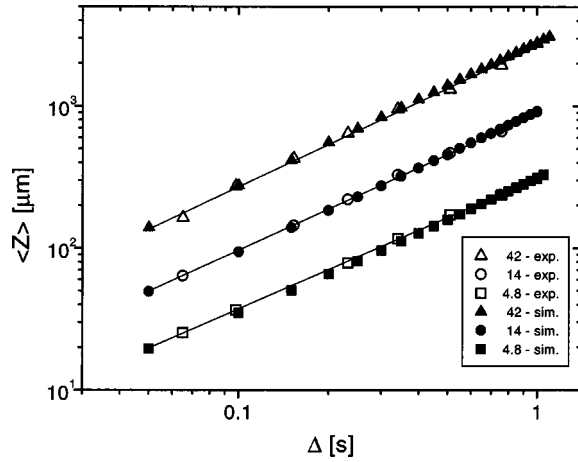


FIG. 6. Average displacement in the flow direction, $\langle Z \rangle$, as a function of time for experimental (open symbols) and simulated data (solid symbols). Solid lines indicate a linear fit to the experimental data. Numbers denote flow rates in ml/min.

discussing its shape and features such as global and local maxima of probability density. For a quantitative description we will first focus our attention on the development of moments of $P_{\Delta}(X, Z)$ with increasing encoding time and their dependence on flow rate and Peclet number.

The general definition of moments of n th order is given as

$$\langle X^n \rangle = \int P(X, Z) X^n dX dZ, \quad \langle Z^n \rangle = \int P(X, Z) Z^n dX dZ. \quad (10)$$

It can be expected that the evolution of moments is entirely determined by the spatial structure of the porous system and the consequent properties of the velocity field. The moments are only indirectly affected by the time variable inasmuch as it separates regimes where diffusion and flow, respectively, are dominant for the resulting mean-squared displacements or second moments. For the first moment, however, a simple relationship is found:

$$\langle X \rangle = 0, \quad (11)$$

$$\langle Z \rangle = \overline{v^*} \Delta = \frac{Q}{\epsilon A} \Delta, \quad (12)$$

where Q is the flow rate and A the cross-section of the sample. The average interstitial velocity $\overline{v^*}$ is also known as the Dupuit-Forcheimer velocity [34], and is a well-defined quantity as the setup of the experiment guarantees a constant flow rate Q and thus a constant $\overline{v^*}$. The average displacement in the flow direction, $\langle Z \rangle$, must then be proportional to time as the contribution due to self-diffusion remains zero for all times. As no net flow occurs in X , and Brownian motion leads to an isotropic spreading in all directions, $\langle X \rangle$ must be zero. The assumption of an isotropic medium seems justified due to the large number of beads ($\sim 1.7 \times 10^5$) although the local porespace favors anisotropic spreading. The smaller number of unit cells in the simulation, containing only 150 beads, can give rise to a certain asymmetry which

leads to nonzero first moments $\langle X \rangle$. This effect, however, can be controlled, and is avoided when centered moments are analyzed.

In Fig. 6, the average displacements $\langle Z \rangle$ obtained from experimental data and from the simulations are compared for all three flow rates. Both sets coincide satisfactorily. The slope of the experimental data yields an interstitial velocity of $(3.1 \pm 0.1) \times 10^{-4}$ m/s for the flow rate 4.8 ml/min, $(8.6 \pm 0.2) \times 10^{-4}$ m/s for 14.0 ml/min, and $(2.53 \pm 0.05) \times 10^{-3}$ m/s for 42.0 ml/min, respectively. Given the dimensions of the system, this leads to an effective porosity of the sample of $(\epsilon = 45 \pm 2)\%$, in good agreement with the value assumed for the simulated random sphere packing.

From the above result, it can be concluded that the first moment $\langle Z \rangle$ in fact scales linearly with time Δ ; in all further discussions, the time variable can therefore be replaced by the average displacement in the flow direction.

The second moments of displacements parallel and perpendicular to the pressure gradient, $\langle Z^2 \rangle$ and $\langle X^2 \rangle$, contain contributions from both Brownian motion and convection. The second moment from self-diffusion alone is isotropic and given by the relation

$$\langle X^2(\Delta) \rangle = \langle Z^2(\Delta) \rangle = 2D(\Delta)\Delta. \quad (13)$$

For an infinite isotropic medium, $D(\Delta)$ is a time-independent constant and equal to the self-diffusion coefficient D_0 . Diffusion within a restricted geometry shows a more complicated pattern. While for displacements much smaller than the wall separation, $D \rightarrow D_0$ is found, displacements much larger than both the average pore size and the correlation length of the pore space lead to a constant self-diffusion coefficient reduced by a certain factor which depends on the porosity and the tortuosity of the system [35]. In the intermediate range, $D(\Delta)$ can be expressed [36] by the short-time expansion

$$\frac{D(\Delta)}{D_0} = 1 - \frac{4}{9\sqrt{\pi}} \frac{S}{V} \sqrt{D_0 \Delta} + \mathcal{O}(\Delta), \quad (14)$$

where S and V are the surface area and the volume of the porous system. However, for the glass bead system investigated in this study, a significant decrease of $D(\Delta)$ can only be expected for times in the order of 1 s, where the influence of flow is already dominating.

Taking flow into account, in the limit of infinite times, the propagator is expected to become a Gaussian centered at $X = 0$ in the X direction and a Gaussian shifted by the average displacement $Z_0 = \overline{v^*} \Delta$ in the Z direction. It has been shown that the shape of the propagator becomes roughly Gaussian for average displacements much larger than the bead size in systems similar to the one investigated in this work [19,24]. However, as we are interested in the intermediate regime where this limit is not yet reached, we investigate the time dependence of the second moments of X and Z .

The spreading of the propagator in X and Z is best monitored by looking at the centered second moments $\langle (X - \langle X \rangle)^2 \rangle$ and $\langle (Z - \langle Z \rangle)^2 \rangle$. While the former is identical to $\langle X^2 \rangle$ as $\langle X \rangle = 0$, the latter describes the spreading of the probability density distribution around the center at $\langle Z \rangle = \overline{v^*} \Delta$. A plot of the centered second moments is shown in

$=1$ is again reached asymptotically for very large displacements exceeding 10 mm, reflecting the limiting pseudorandom walk character of the displacement distributions expected at long times. In between, a maximum in γ is found at a displacement which depends on the Peclet number, and is shifted toward larger average displacements for smaller Pe. γ is generally larger for $\langle(Z-\langle Z \rangle)^2\rangle$ than for $\langle(X-\langle X \rangle)^2\rangle$. For the highest flow rate used in this study, $\gamma=2$ is almost reached, which can be expected to be the maximum value possible; it is considerably less for the smaller flow rates. Note the minimum $\gamma < 1$ in $\langle(X-\langle X \rangle)^2\rangle$ occurring at $\langle Z \rangle \approx 1$ mm. This minimum might be related to the particular shape of the two-point correlation function of the matrix which possesses a negative region (“anticorrelation”) between 0.9 and 2.0 bead radii for a random packing of monosized spherical particles [26]. Indeed, $\langle Z \rangle$ at the position of the minimum corresponds to an average transverse displacement $\sqrt{\langle(X-\langle X \rangle)^2\rangle}$ of about $350 \mu\text{m}$ or 1.2 bead radii [see Fig. 7(a)].

While this is not a sufficient model for the system studied here, it is of interest to compare the behavior of $\langle(Z-\langle Z \rangle)^2\rangle$ with that predicted for Taylor dispersion for flow between parallel plates [37], i.e.,

$$\langle(Z-\langle Z \rangle)^2\rangle = \left(2D_0 + \frac{\bar{v}^{*2}a^2}{\pi^2 D_0}\right)\Delta - \frac{\bar{v}^{*2}a^4}{\pi^4 D_0^2}(1 - e^{-\pi^2 D_0 \Delta/a^2}). \quad (16)$$

The limiting cases are found to be

$$\langle(Z-\langle Z \rangle)^2\rangle = \begin{cases} 2D_0\Delta + \frac{1}{2}\bar{v}^{*2}\Delta^2 + \mathcal{O}(\Delta^3), & \Delta \ll a^2/D_0 \\ \left(2D_0 + \frac{\bar{v}^{*2}a^2}{\pi^2 D_0}\right)\Delta + \mathcal{O}(1), & \Delta \gg a^2/D_0. \end{cases} \quad (17)$$

A crossover from $\gamma=1$ to $\gamma=2$ is observed for short displacements, equivalent to short times where $\Delta \ll a^2/D_0$ whereas a decrease of γ back toward $\gamma=1$ is predicted for the condition $\Delta_c \gg a^2/D_0$. The observed behavior is qualitatively similar to the classical Taylor dispersion, showing a crossover from $\gamma=1$ to 2 at a time scale when the flow effect on the mean-squared displacement becomes dominant over Brownian motion. At larger $\langle Z \rangle$, when the spreading of the propagator almost behaves as in the case of pure directed flow, hence $\gamma \approx 2$, this similarity is lost as the spreading is now dominated by the pseudorandom walk caused by flow around the obstructions of the porous solid.

A comparison of the spreading of the particle probability density function due to flow and as a consequence of Brownian motion is achieved by determining the ratio of the components of the dispersion tensor \mathbf{D}^* and the self-diffusion coefficient D_0 . The dispersion tensor \mathbf{D}^* can be regarded as a function of time and therefore average displacement:

$$\mathbf{D}^* = \mathbf{D}^*(\Delta) = \mathbf{D}^*(\langle Z \rangle). \quad (18)$$

It is defined by

$$\mathbf{D}^* = \frac{d\langle(\mathbf{R}-\langle\mathbf{R}\rangle)^2\rangle}{d\Delta}, \quad (19)$$

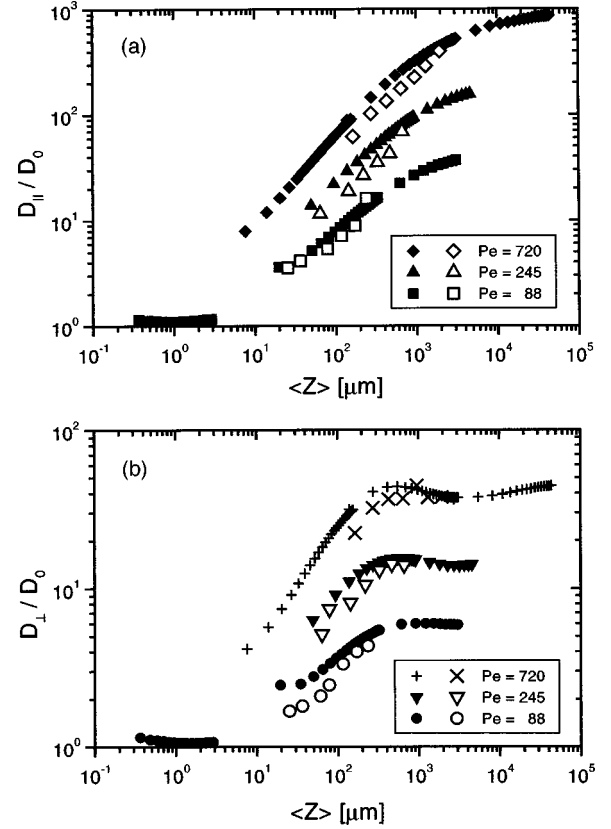


FIG. 8. Ratio of dispersion coefficients to the self-diffusion coefficient D_0 for experimental and simulated data. (a) Parallel to the flow direction, $D_{||}^*(\langle Z \rangle)$. (b) Perpendicular to the flow direction, $D_{\perp}^*(\langle Z \rangle)$.

where $\langle(\mathbf{R}-\langle\mathbf{R}\rangle)^2\rangle$ is the centered second moment in three dimensions. In an isotropic porous medium with an interstitial velocity \bar{v}^* parallel to the z axis, \mathbf{D}^* can be decomposed into parallel and transverse components [11]

$$\mathbf{D}^* = \begin{pmatrix} D_{\perp}^* & 0 & 0 \\ 0 & D_{\perp}^* & 0 \\ 0 & 0 & D_{||}^* \end{pmatrix}. \quad (20)$$

The dispersion tensor remains time dependent as long as $\gamma \neq 1$.

In Fig. 8, the components of the dispersion tensor perpendicular and parallel to the flow direction are compared for the three different flow rates used in this study. D_{\perp}^* is found to become constant for average displacements $\langle Z \rangle \gtrsim 300\text{--}400 \mu\text{m}$, a value that seems to be roughly independent of the Peclet number. From this point on, the displacements in X are spreading in a way that is characteristic for a Gaussian propagator. In their treatment of dispersion, Koch and Brady [8] suggested that D_{\perp}^* was determined entirely by mechanical contributions and estimated that it would reach its limiting value in a time $\Delta_c = a/(v^*\Phi^{1/2})$, where Φ is the solids volume fraction. This time is equivalent to $\langle Z \rangle = a/\Phi^{1/2}$ which for $\Phi=0.55$ gives $\langle Z \rangle = 800 \mu\text{m}$ for the grain diameter of $a = 600 \mu\text{m}$. This is within a factor of 2 of the values represented in Fig. 8(b).

$D_{||}^*$ approaches its asymptotic limit much more slowly than D_{\perp}^* , and does not become constant within even the

range of the simulations. For the highest flow rate of 42 ml/min, D_{\parallel}^* is still changing for average displacements $\langle Z \rangle$ exceeding 100 bead radii. The limiting values of D_{\parallel}^* can, however, be estimated reasonably well; they fall in the same range as results presented in the literature (see Ref. [20] for a compilation). The characteristic time at which the longitudinal dispersion coefficient becomes roughly constant can be estimated from the simulated data to about 20 s; this is in good agreement with relations given in the literature, where the quantity $D_0 \Delta / L^2$ is of order unity [38]. Koch and Brady [8] derived expressions for the time required for the nonmechanical contributions to longitudinal dispersion to reach their asymptotic limits. The mechanism of relevance to this study is the so-called boundary layer dispersion arising from the nonslip condition of the velocity field at the walls of the solid matrix. The time for this process to reach its asymptotic limit is of order $a Pe^{1/3} / \bar{v}^*$ which, when converted into values of $\langle Z \rangle$ appropriate to the three velocities used here, give $\langle Z \rangle$ in the range $(3-5) \times 10^3 \mu\text{m}$. This can be seen to underestimate the values suggested by the simulation results in Fig. 8(a). The latter are supported by the experimentally derived data in that, at the limit of the experiments, corresponding to $\langle Z \rangle \approx 10^3 \mu\text{m}$, there is no sign of approach to asymptotic behavior.

In Ref. [20], in which the dispersion coefficient was determined by PGSE NMR from the low- q data, a much faster approach toward $D_{\parallel}^*(\Delta) \approx \text{const}$ was found for a similar system of spherical beads. An identical analysis of the measurements presented in this work led to the same values of $D_{\parallel}^*(\Delta)$ as those obtained from the full propagator, as described above, and we are unable to offer any explanation for this difference.

The dependence of the dispersion coefficients on Peclet number has been written [39] in the dimensionless power-law form

$$D_{\parallel}^*/D_0 \propto Pe^{\alpha}. \quad (21)$$

For Pe much larger than unity, $\alpha=2$ is found if diffusion is the predominant mixing effect between different velocities, as is the case for dispersion in laminar flow in a capillary tube. If velocity variations within the network are the main cause for dispersion, $\alpha=1$ is observed. For a system containing regions where the fluid velocity is large and others where it is small, an intermediate behavior is expected [11]. In Ref. [26], flow through systems containing either spherical or ellipsoidal particles with a wide range of aspect ratios was simulated numerically. An average relationship of $D_{\parallel}^*/D_0 = 0.26 Pe^{1.29}$ and $D_{\perp}^*/D_0 = 0.27 Pe^{0.72}$ was found for $Pe \geq 10$, which coincides well with the values in this study. In particular, the proportionality $D_{\parallel}^*/D_{\perp}^* \propto Pe^{1/2}$ [40] is found to a good approximation [see Figs. 8(a) and 8(b)].

C. Residence time distributions (RTD's) from PGSE NMR

The displacement distributions, such as $P_{\Delta}(Z)$, derived from PGSE NMR, are formally equivalent to the tracer distributions which are used to characterize fluid transport through porous solids [14,15]. In particular, $c_{\tau}(Z)$ displayed in Fig. 2 of Ref. [14] correspond exactly to the $P_{\Delta}(Z)$ determined by the NMR experiments described in this paper and

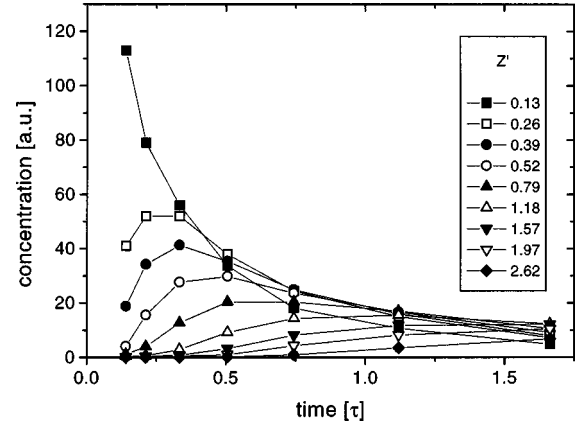


FIG. 9. The residence time distribution $c_{\tau}(Z')$ as a function of τ for flow through a 600- μm glass bead pack at 14 ml/min. The definitions of Z' and τ are dimensionless as given in Ref. [14]: $Z' = Zk^{-1/2}$ and $\tau = \langle Z \rangle k^{-1/2}$, where $k^{1/2} = \frac{2}{9} \Phi^{-1} a^2$ is the screening length. The corrected Peclet number according to Ref. [14] is $Pe' = \bar{v}^* k^{1/2} / D = 150$.

elsewhere [16–25]. As with $c_{\tau}(Z)$, which allow the calculation of tracer RTD's, $c_Z(\tau)$, so the $P_{\Delta}(Z)$ give access to the equivalent NMR determined RTD's. The formal equivalence requires the assumption that the distributed labeling of molecular positions by NMR is the same as the infinitely thin, infinite area transverse labeling assumed in tracer measurements. All that is required is that, as the NMR method measures displacements, the distribution of initial labeling is representative of all locations in the fluid phase. Based on their nonlocal formulation of the transport problem in porous solids, Koch and Brady calculated $c_{\tau}(Z)$ and $c_Z(\tau)$ for a Peclet number of 100 and a solids fraction of 0.5 which are similar to those used in this study. It is clear from previously published data, e.g., Refs. [18–25] that the calculated $c_{\tau}(Z)$ shown in Fig. 2 of Ref. [14] show little agreement with those observed experimentally. We have used our data to calculate RTD's for the 600- μm glass sphere bed using the same definitions of variables as used by Koch and Brady [14]. Figure 9 shows these NMR-derived RTD's for the flow rate corresponding to $Pe=245$ ($Pe'=150$ according to the screening-length corrected definition of Ref. [14]) and $\Phi=0.55$. It can be seen by comparison with Fig. 3 in Ref. [14] that there is little similarity, even qualitatively, with the predictions of the theory.

D. Correlation between displacements in X and Z

The principal aim of this paper is to show that our NMR experiment gives direct information on correlations between axial and transverse components of the fluid transport. The centered second moments are generally found to be larger along the pressure gradient than perpendicular to it. In fact, they show a mutual dependence for long times when the limit of Gaussian propagators is reached. However, as will be pointed out later, the moments $\langle (X - \langle X \rangle)^2 \rangle$ and $\langle (Z - \langle Z \rangle)^2 \rangle$ are not correlated for $\Delta \rightarrow \infty$ in the strict mathematical sense, despite this proportionality.

The centered second moments represent averaged quantities for the whole system, and do not sufficiently describe the actual connection between displacements in both directions.

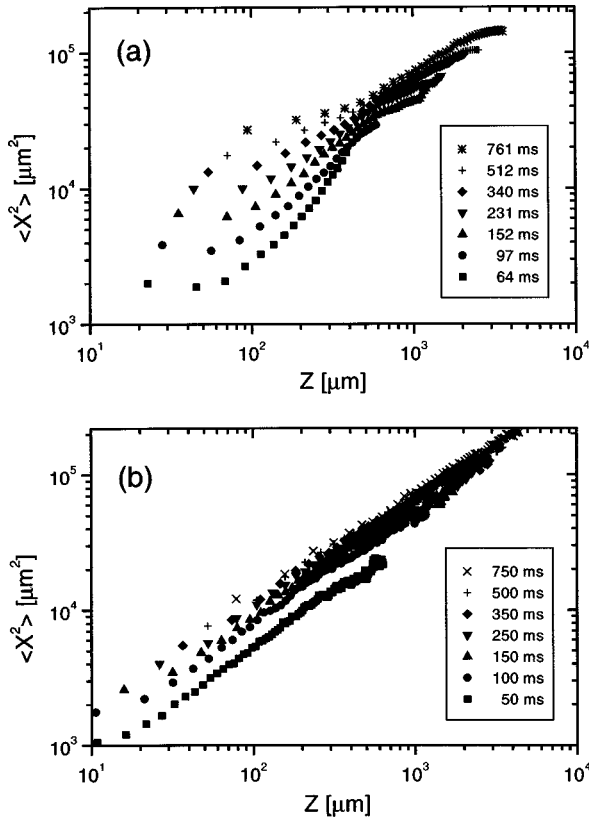


FIG. 10. Mean-squared displacement perpendicular to the flow direction, $\langle X^2 \rangle$, as a function of displacement Z . The moments have been calculated from the two-dimensional propagators. (a) Experimental data as shown in Fig. 3. (b) Simulated data as shown in Fig. 5.

In particular, one would like to know if, for a given encoding time, a spin-bearing particle that has traveled a larger-than-average distance in the flow direction is also expected to have a larger-than-average displacement in the perpendicular direction. In other words: are large displacements in Z correlated with large displacements in X or not?

A way to gain insight into this question is to compute the second moments $\langle X^2 \rangle$ as a function of Z . One thereby chooses a subset of particles that have reached, by different pathways, a displacement between Z and $Z + dZ$ after a time interval Δ . The inverse approach of plotting $\langle (Z - \langle Z \rangle)^2 \rangle$ vs X is also justified, but less illustrative.

Figure 10(a) shows a superposition of the experimental data for 42 ml/min, as compared to the simulations in Fig. 10(b). In Fig. 10(a), it can be seen that $\langle X^2 \rangle$ (which is identical to the centered second moment) is only weakly dependent on Z for small Z as this region is dominated by self-diffusion which is isotropic. The slope then rises monotonically toward larger Z with all values of Δ achieving an approximately common slope in the log-log plot.

The fact that the curves for different times are nearer to each other in the simulated data as compared to the experimental ones is a consequence of the sharper and more persistent peak around zero already mentioned. It has the effect that “static” and “flowing” particles are more strongly separated than in the experimental case. Thus the diffusion-dominated region (where $\langle X^2 \rangle$ scales with time and therefore with $\langle Z \rangle$) is restricted to a smaller X and Z .

From the simulation it is clear that for displacements much larger than the diffusion range, $\langle X^2 \rangle$ follows a power-law dependence of Z . The slope in the log-log plot is found to be 0.74 ± 0.02 both in the experimental and the simulated data for $Z \geq 500 \mu\text{m}$. While for small Z , isotropic self-diffusion is dominating and X and Z are uncorrelated, there remains a positive correlation between both quantities throughout the full range of Z .

The quantification of correlations for the entire range of displacements is necessarily connected with the reduction of specific properties onto a single characteristic figure. The proper mathematical definition of the correlation coefficient which relates two parameters A and B , $\rho_{A,B}$, is given as follows:

$$\rho_{A,B} = \frac{\text{cov}(A,B)}{\sqrt{\text{Var}(A)}\sqrt{\text{Var}(B)}}, \quad (22)$$

where covariance and variance are defined as

$$\text{cov}(A,B) = \langle AB \rangle - \langle A \rangle \langle B \rangle, \quad (23)$$

$$\text{Var}(A) = \langle A^2 \rangle - \langle A \rangle^2, \quad (24)$$

and where $\langle A \rangle$, for example, is given by

$$\langle A \rangle = \int_{-\infty}^{\infty} \int_{-\infty}^{\infty} P(A,B) A \, dA \, dB. \quad (25)$$

Both experimental and simulation results are subject to noise that makes the calculation of higher moments increasingly inaccurate. One is therefore interested in the simplest possible correlation relations, such as

$$\rho_{|X|,Z}, \quad \rho_{|X|,Z^2}, \quad \rho_{X^2,Z}, \quad \rho_{X^2,Z^2}.$$

It was found that the general features of these quantities and their evolution with time and flow rate remain the same while only the absolute values are changed slightly.

Figure 11(a) compares the correlation coefficients $\rho_{X^2,Z}$ for the experimentally obtained propagators. Correlations are generally larger for high flow rates, i.e., larger Peclet numbers. Furthermore, an increase of the correlation coefficient with $\langle Z \rangle$ is found for 4.8 ml/min, a decrease for 42.0 ml/min, and an intermediate behavior showing a maximum for 14.0 ml/min. Despite an estimated error of up to $\pm 10\%$ in the absolute values, the maximum seems to appear for $\langle Z \rangle$ between 100 and 300 μm for 14.0 ml/min.

The interpretation becomes clearer by considering the $\rho_{X^2,Z}$ derived from the simulated propagators. These are shown in Fig. 11(b), and cover a wider range of displacements than the experimental data. The dependence on flow rate is obvious. A maximum is clearly seen at displacements near to the bead radius. Additional simulations for 4.8 ml/min have been run with self-diffusion coefficients of $D_0/100$ and $D_0/10000$ in order to reveal the effects of flow alone, and these are included in Fig. 11(b).

From the behavior of the correlation coefficient, the following interpretation can be drawn. At very short times, particle displacements are dominated by Brownian motion on scales much smaller than the bead size. This motion is random and isotropic, and generates no correlation between dis-

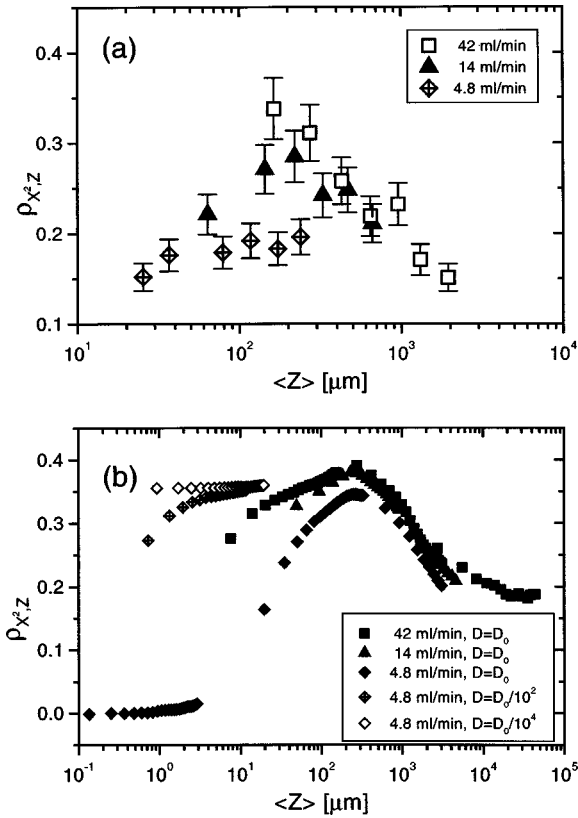


FIG. 11. (a) Correlation coefficients $\rho_{X^2,Z}$ for experimentally obtained two-dimensional propagators. Errors bars are estimated to 10% from the scattering of the computed ρ values. (b) Correlation coefficients $\rho_{X^2,Z}$ for two-dimensional propagators obtained by simulation. Open symbols indicate simulations at reduced self-diffusion coefficients of $D_0/100$ and $D_0/10\,000$, respectively.

placements in X and Z . For larger times, the motion is increasingly influenced by the velocity field in the pore space, with its preferred direction along the pressure gradient. The velocity field represents the way fluid particles probe the spatial structure of the pore space under the constraints of the boundary conditions. The local velocity distributions in a pack of glass spheres were discussed in Ref. [41]; regions of large and small local velocities could be identified which indicate the position of the particles with respect to the main flowlines. It is clear that larger Peclet numbers allow fewer particles to change between these pools in a given time, resulting in larger correlation coefficients at any given displacement. For very small self-diffusion coefficients, motions become dominated by the flow field, as is clear from Fig. 11(b).

At a characteristic length scale, fluid molecules will have to change their flow direction or exchange between the pools of large and small velocity; the persistence length of a streamline must be connected to the typical structural size of the system, and for very large displacements it becomes increasingly unlikely for a particle to flow in its initial direction. One would therefore expect a maximum of the correlation coefficient that is intimately related to the characteristic length scale, which is given by the bead size in this system. Note that in the complete absence of Brownian motion, the correlation coefficient will start off as a constant, the value of

which is solely determined by the spatial structure of the velocity field. It will start to decrease when the average displacement $\langle Z \rangle$ exceeds the persistence length, the observed maxima in Figs. 11(a) and 11(b) being a consequence of the combined effect of Brownian motion and flow.

For very large displacements, a complete loss of correlation is expected as the dispersion in both X and Z becomes determined by the pseudodiffusive character of the displacements. Note that although the latter condition is almost met for the largest displacements in the simulation, which is indicated by a Gaussian-like shape of the marginal propagators, the correlation coefficient has not yet fallen close to zero.

The peak in the correlation coefficient is remarkably well pronounced in the experimental data, given the fact that a polydispersity of the real glass beads exists. However, while the absolute values of ρ in the experimental and in the simulated data sets are comparable for the largest flow rate, the dependence on the Peclet number is more pronounced in the experiment. Given that D , v^* , and the bead diameter are identical, and that edge effects are not expected to play any role for the displacements observed, deviations of the simulated from the real velocity field must be assumed which affect small flow rates most. This feature might be connected to an observation of the peak near zero displacement that is more persistent in the simulation than in the experimental results: a larger fraction of particles possessing both small X and small Z has to influence the absolute value of the correlation coefficients.

The observation of a positive correlation between X and Z suggests the concept of a preferential flow direction, or, more precisely, a direction which is more probable to find than others. For example, the probability density of particles remaining near $X \approx 0$ decreases for larger displacements Z . In order to visualize the geometrical properties of this correlation, we write the joint probability density as the sum of the product of its marginals and a function that incorporates the correlation between the measured quantities:

$$P_{\Delta}(X,Z) = P_{\Delta}(X)P_{\Delta}(Z) + C_{\Delta}(X,Z). \quad (26)$$

The correlation matrix $C_{\Delta}(X,Z)$ contains only zero elements if displacements in X and Z are mutually independent. This case is realized for Brownian motion in an isotropic system where

$$P(X,Z) = \frac{1}{2\pi\sigma_X\sigma_Z} \exp[-(X-X_0)^2/(2\sigma_X^2)] \\ \times \exp[-(Z-Z_0)^2/(2\sigma_Z^2)].$$

However, if X and Z are correlated, a plot of $P(X,Z) - P(X)P(Z)$ renders the correlation matrix directly.

This operation has been performed for the propagators in Fig. 4, and is presented in Fig. 12 for the experimental data. Simulated data result in equivalent plots. Compared to the actual propagators in Fig. 4, the difference propagators show a much larger amount of structure. One observes a fourfold symmetry: a positive peak for small X and Z develops into a narrow negative region for large Z and small X as well as for large X and small Z . For intermediate values of X and Z , the sign of $C_{\Delta}(X,Z)$ is again positive, and its local maximum

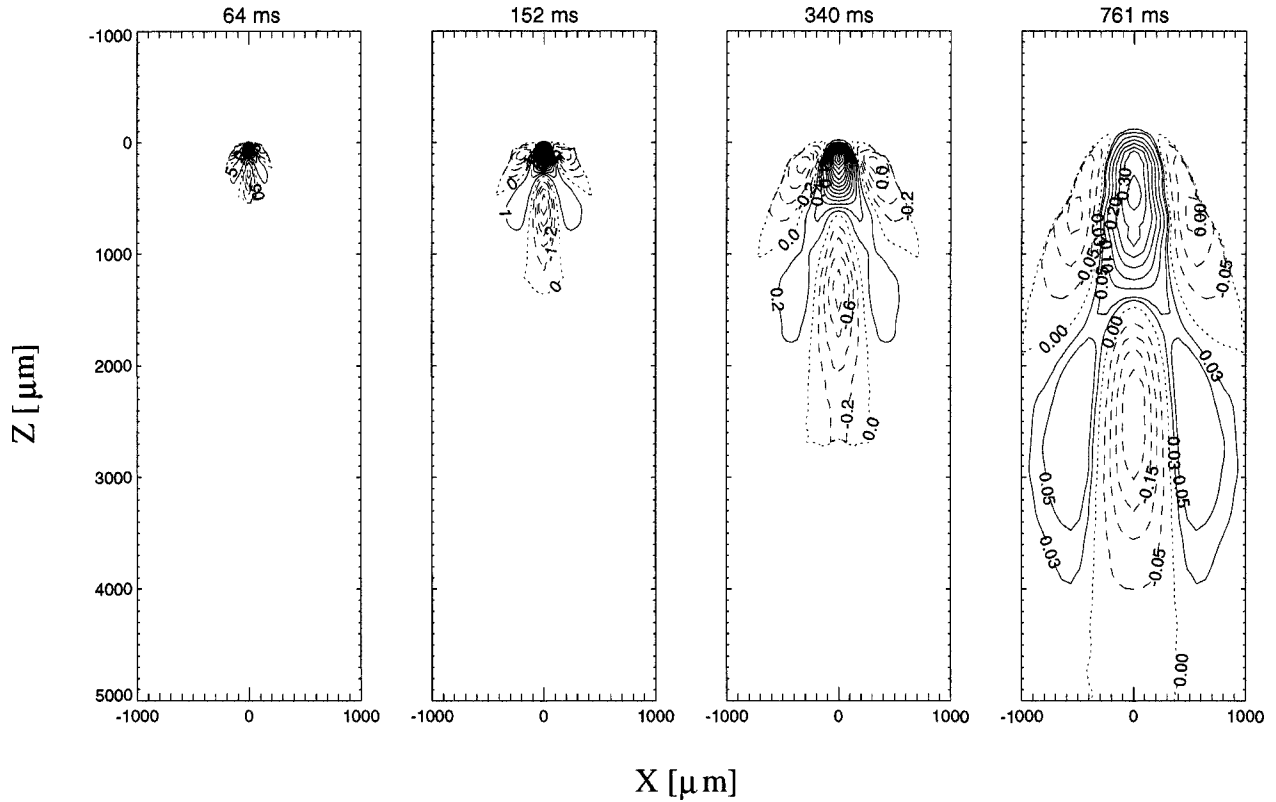


FIG. 12. Difference propagator $C_{\Delta}(X,Z) = P_{\Delta}(X,Z) - P_{\Delta}(X)P_{\Delta}(Z)$ for experimental data at a flow rate of 42.0 ml/min, axis scales in μm . Contour lines are drawn from approximately ± 0.05 of the peak intensity in linear spacing; numbers indicate probability densities in 10^4 m^{-2} using the normalization of Fig. 4. Positive values are indicated by solid lines, and negative values by dashed lines. Dotted lines represent $C_{\Delta}(X,Z) = 0$. Data are cut at points where $P_{\Delta}(X,Z)$ is typically below 0.02 of its peak value to avoid contributions by noise; this determines the outer bounds of the $C_{\Delta}(X,Z) = 0$ line.

describes a line that is curved in the flow direction. These general features are independent of the parameters in the experiment or the simulation and have been observed before for flow in porous sandstone rocks [27]. It is also found for short-time simulations for average displacements down to a few micrometers. However, for a diffusion coefficient reduced by a factor of 10^4 in the simulations, the features become much sharper, revealing the initial state of the velocity field before spreading due to self-diffusion or changes in local flow directions lead to a broadening in the correlation matrix picture. The absolute magnitude in the correlation plot, on the other hand, decreases with longer encoding times (see numbers at contour lines in Fig. 12) due to the general spreading of the probability density function. This is analogous to the spreading of the propagator $P_{\Delta}(X,Z)$ itself.

The correlation matrix can be understood as a function that identifies regions of correlations larger or smaller than the reference state $P_{\Delta}(X)P_{\Delta}(Z)$ which formally defines the independence of the variables X and Z . However, as pointed out by Wadsworth and Bryan [42], while the use of a function such as $C_{\Delta}(X,Z)$ gives a clear answer to whether the variables X and Z are correlated or not, the “mathematical representation of the relationship, once demonstrated, is an art in itself.” That said, it is clear that, because of normalization of the propagators in general, the integral over $C_{\Delta}(X,Z)$ must be zero, which necessitates a particular sym-

metry and a sign change at certain coordinates. A simplified view of $C_{\Delta}(X,Z)$ might lead to an interpretation of the ridges of positive values as the lines of preferential displacements. One would then conclude that fluid molecules would preferably flow along a certain angle θ_{max} relative to the X axis, while, for $\theta \approx 0^\circ$ and $\theta \approx 90^\circ$, displacements are less likely to be found. One possible definition of θ_{max} employs determining the maximum of the radial first moment, $\langle R(\theta) \rangle$, with respect to the origin at $\{X,Z\} = 0$. While θ_{max} is not found to be significantly influenced by the flow rate for the case investigated in this study, it is certainly a function of the ratio of the average displacements in z and x directions. We are currently considering in more detail the significance of $C_{\Delta}(X,Z)$ and the role of the reference state $P_{\Delta}(X)P_{\Delta}(Z)$ in its definition and physical interpretation.

E. Comparison with model systems

Another approach towards a better understanding of the meaning of correlations between displacements can be obtained by performing independent simulations and assuming model propagators. One case which can be solved analytically assumes a Gaussian propagator along X for each point in Z , the variance of which scales with a power of Z :

$$P(X,Z) = \frac{4}{\sqrt{\pi\lambda}\beta^{(\alpha+1)/2}\Gamma\left(\frac{\alpha+1}{2}\right)} e^{-Z^2/\beta} e^{-X^2/(\lambda Z^{2\alpha})}. \quad (27)$$

This propagator fulfills the normalization condition $\iint P(X,Z)dX dZ=1$ when defined for positive X and Z only. The general moments are represented by

$$\langle X^n Z^m \rangle = \frac{\lambda^{n/2} \beta^{(m/2) + (\alpha/2)n} \Gamma\left(\frac{n+1}{2}\right) \Gamma\left(\frac{m}{2} + \frac{\alpha}{2}n + \frac{\alpha+1}{2}\right)}{\sqrt{\pi}\Gamma\left(\frac{\alpha+1}{2}\right)}, \quad (28)$$

the correlation coefficients are given by

$$\rho_{X^n, Z^m} = \frac{\Gamma\left(\frac{n+1}{2}\right) \left[\Gamma\left(\frac{m}{2} + \frac{\alpha}{2}n + \mu\right) \Gamma(\mu) - \Gamma\left(\frac{\alpha}{2}n + \mu\right) \Gamma\left(\frac{m}{2} + \mu\right) \right]}{1 \sqrt{\Gamma\left(n + \frac{1}{2}\right) \Gamma(\alpha n + \mu) \Gamma(\mu) \sqrt{\pi}} - \Gamma^2\left(\frac{n+1}{2}\right) \Gamma^2\left(\frac{\alpha}{2}n + \mu\right)} \Bigg/ \sqrt{\Gamma(m + \mu) \Gamma(\mu) - \Gamma^2\left(\frac{m}{2} + \mu\right)} \quad (29)$$

where $\mu = (\alpha+1)/2$. For $\alpha=0$, all correlation coefficients are equal to zero, as expected. Note that the correlations do not depend on the parameters β and λ . The dependence of $\rho_{X,Z}$ and $\rho_{X^2,Z}$ on α are shown in Fig. 13.

Numerical computations of this model propagator have been performed employing a MatLab routine; the resulting moments and correlations were found to match with the theoretical values within less than 1%, depending on the resolution of the calculation. The findings in Sec. VI D, shown in Fig. 10, suggest $2\alpha=0.74$. The propagator and the correlation matrix for this parameter are shown in Fig. 14. The similarity to the bead system investigated in this study is striking at first sight. The main difference between model and experiment lies in the short-displacement behavior. The marginal $P(Z)$ of the distribution of Eq. (27) has the form

$Z^\alpha e^{-Z^2}$. Although similarities between the experimentally obtained propagator $P(Z)$ and this distribution might exist, the persistent peak of high probability density near the origin cannot be represented. Also, the expected Gaussian shape of $P(Z)$ for long times is not realized by the model. Nevertheless, the general properties of the correlation matrix coincide reasonably well with both the experimental and simulated data presented above. Tentative analyses of flow through other porous media lead to similar characteristics, but with an exponent 2α considerably different from the one obtained for packed glass beads [43]. A model propagator in this or a modified form can therefore serve for the discussion and comparison of general features of the spreading process in X and Z , while certain details such as the small-displacement and long-time behavior contain additional information about the characteristics of the specific system.

In an attempt to gain some further insight into the influence of local pore geometry on the form of the joint probability density, we have analyzed the probability densities generated by the simple two-bond capillary model, described earlier, for a series of values of the angle α in the range $0^\circ - 80^\circ$ with $\Delta v_{\max}(\theta=0) = 2l$. Clearly the dependency of the probability density on α will be confined to regions where the displacement exceeds the length l of the initial capillary; as the probability density is small in those regions, we expect the linear correlation coefficient and first moment to be relatively insensitive to variations in α . We have therefore calculated the ratio $\langle (X - \langle X \rangle)^2 \rangle / \langle (Z - \langle Z \rangle)^2 \rangle$ as a function of α . We find for this model that

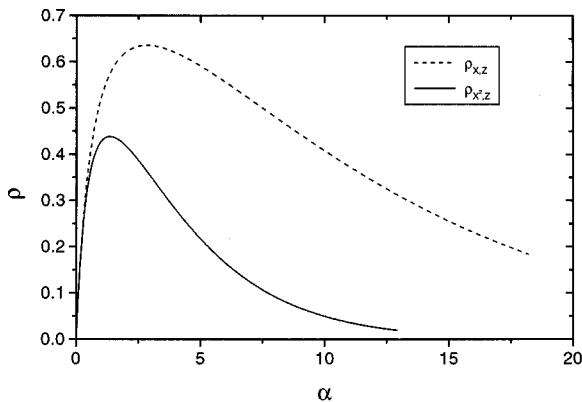


FIG. 13. Correlation coefficients $\rho_{X,Z}$ and $\rho_{X^2,Z}$ for the model propagator described in the text [Eq. (27)] as a function of the parameter α .

$$\frac{\langle (X - \langle X \rangle)^2 \rangle}{\langle (Z - \langle Z \rangle)^2 \rangle} = 0.287 + 0.178(1 - \cos \alpha). \quad (30)$$

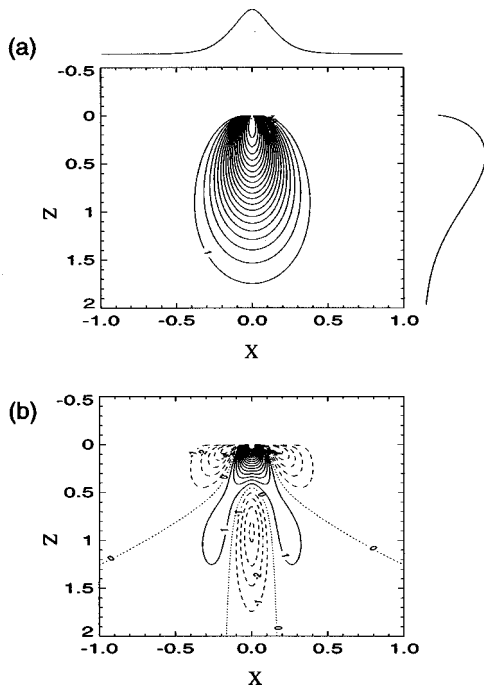


FIG. 14. (a) Two-dimensional propagator $P(X,Z)$ for the model described in the text [Eq. (27)]; $2\alpha=0.74$. Contour lines are drawn from 0.05 of the peak intensity in linear spacing. (b) Correlation matrix $C(X,Z)=P(X,Z)-P(X)P(Z)$ for the plot in (a). Contour lines are drawn from ± 0.005 of the peak intensity in nonlinear spacing. Positive values are indicated by solid lines, and negative values by dashed lines. Dotted lines represent $C(X,Z)=0$.

To compare this result to our experimental and simulated data, it is necessary to relate the bond length l to the characteristic length scale in our sample. We take $l=L/3$; this choice, although inevitably to some extent arbitrary, is physically reasonable and gives values for $\langle Z \rangle$ and $\langle (Z - \langle Z \rangle)^2 \rangle$ in the ranges 58–65 μm and 4000–6100 μm^2 , respectively, consistent with the data presented in Fig. 7(a).

The second-moment ratios for our experimental and bead-pack simulation data are almost independent of $\langle Z \rangle$ in the range of $\langle Z \rangle$ under consideration. They do however depend upon Peclet number, ranging from 0.5 for $\text{Pe}=88$ to an apparent limit of 0.4 for $\text{Pe}>250$, when spreading is dominated by convective transport. The limiting value is the most appropriate for comparison with our model, which neglects effects due to diffusion; Eq. (30) then yields a value of $\approx 70^\circ$ for α . That value is not unreasonable—for example, in a hexagonal close-packed structure fluid elements experience a change in direction of 72° between entering and leaving a tetrahedral “pore.” However, in view of the simplicity of our model and the fact that random packing must lead to a distribution of pore geometries, we must regard this result as merely illustrative of the sort of pore scale structural information which could be extracted from the form of the joint density at small displacements.

VII. CONCLUSIONS

The joint probability distribution for displacements parallel and perpendicular to the net flow direction have been

determined experimentally for water flow in a system of packed glass beads. Numerical simulations have been carried out for a wider range of average displacements than was accessible by experiment.

The simulations, obtained by successively generating a random packing of spherical beads, solving the Stokes equation, and monitoring of the displacements of particles randomly distributed in the pore space, have been shown to agree reasonably well with the experimental results. The major part of the deviations can be explained by a different spreading behavior of a fraction of particles remaining near their starting positions.

The evolution of second moments of the displacement distributions as a function of flow rate and encoding time shows the crossover from a regime dominated by Brownian motion to an asymptotical approach toward propagators of Gaussian shape. The limiting dispersion for long times is reached much earlier in X compared to Z . The dependence of the dispersion coefficient \mathbf{D}^* on the Peclet number suggests an intermediate behavior where the mixing process is dominated by velocity variations but contains a non-negligible contribution from self-diffusion.

The mean-squared displacement perpendicular to the flow direction follows a power-law dependence on Z for large Z . From the full joint probability propagator representation, a correlation between X^2 and Z is found that decreases for average displacements in the flow direction $\langle Z \rangle$, larger than a characteristic length equivalent to the bead radius, while decreasing again for much smaller $\langle Z \rangle$ due to the dominating effect of isotropic self-diffusion.

A plot of the correlation matrix $C_\Delta(X,Z)=P_\Delta(X,Z)-P_\Delta(X)P_\Delta(Z)$ possibly indicates preferential directions for displacements by larger-than-average correlation values for a specific region of displacements. The shape of this region changes with increasing flow time. Correlation matrices of similar shape can be generated by appropriate model propagator functions. Numerical simulations have shown that the peculiarities of the matrix shape reflect characteristic structural details such as size and orientation of microcapillaries. Experiments and theoretical analyses are currently being performed to describe a wider range of porous systems by the properties of fluid flow through their pore space [43]. Two-dimensional propagators can be employed to improve the understanding of how fluids spread in a porous network and how this spreading is governed by parameters such as self-diffusion coefficients and flow rates, on the one hand, and porosity, permeability, and tortuosity on the other hand.

ACKNOWLEDGMENTS

One of the authors (S.S.) is indebted to the Deutsche Forschungsgemeinschaft (DFG), (Grant No. Sta 511/1-1) and the Training and Mobility of Researchers (TMR) Programme of the European Union (Grant No. ERBFMBICT961836), for financial support.

- [1] J. J. Fried and M. A. Combarous, *Adv. Hydrosci.* **7**, 169 (1971).
- [2] A. L. Dullien, *Porous Media: Fluid Transport and Pore Structure* (Academic, New York, 1979).
- [3] J. H. Cushman, *Dynamics of Fluids in Hierarchical Porous Media* (Academic, New York, 1990).
- [4] H. D. Pfannkuch, *Rev. Inst. Fr. Pétrole* **18**, 215 (1963).
- [5] D. J. Gunn and C. Pryce, *Trans. Inst. Chem. Eng.* **47**, 341 (1969).
- [6] R. Aris, *Proc. R. Soc. London, Ser. A* **235**, 67 (1956).
- [7] G. I. Taylor, *Proc. R. Soc. London, Ser. A* **219**, 186 (1953).
- [8] D. L. Koch and J. F. Brady, *J. Fluid Mech.* **154**, 399 (1985).
- [9] D. A. Edwards, M. Shapiro, H. Brenner, and M. Shapira, *Transp. Porous Media* **6**, 337 (1991).
- [10] H. P. Amaral Souto and C. Moyne, *Phys. Fluids* **9**, 2253 (1997).
- [11] J. Sallès, J.-F. Thovert, R. Delannay, L. Prevors, J.-L. Auriault, and P. M. Adler, *Phys. Fluids A* **5**, 2348 (1993).
- [12] E. Charlaix, J.-P. Hulin, and T. J. Plona, *Phys. Fluids* **30**, 1690 (1987).
- [13] A. Ding and D. Candela, *Phys. Rev. E* **54**, 656 (1996).
- [14] D. L. Koch and J. F. Brady, *J. Fluid Mech.* **180**, 387 (1987).
- [15] D. L. Koch and J. F. Brady, *Chem. Eng. Sci.* **42**, 1377 (1987).
- [16] P. T. Callaghan, *Principles of Nuclear Magnetic Resonance Microscopy* (Clarendon, Oxford, 1991).
- [17] J. Kärger and W. Heink, *J. Magn. Reson.* **51**, 1 (1983).
- [18] K. J. Packer and J. J. Tessier, *Mol. Phys.* **87**, 267 (1996).
- [19] M. H. G. Amin, S. J. Gibbs, R. J. Chorley, K. S. Richards, T. A. Carpenter, and L. D. Hall, *Proc. R. Soc. London, Ser. A* **453**, 489 (1997).
- [20] J. D. Seymour and P. T. Callaghan, *AIChE. J.* **43**, 2096 (1997).
- [21] H. Van As and D. van Dusschoten, *Geoderma* **80**, 389 (1997).
- [22] J. J. Tessier and K. J. Packer, *Phys. Fluids* **10**, 75 (1998).
- [23] L. Lebon, L. Oger, J. Leblond, J. P. Hulin, N. S. Martys, and L. M. Schwartz, *Phys. Fluids* **8**, 293 (1996).
- [24] J. J. Tessier, K. J. Packer, J.-F. Thovert, and P. M. Adler, *AIChE. J.* **43**, 1653 (1997).
- [25] R. S. Maier, D. M. Kroll, Y. E. Kutsovsky, H. T. Davis, and R. S. Bernard, *Phys. Fluids* **10**, 60 (1998).
- [26] D. Coelho, J.-F. Thovert, and P. M. Adler, *Phys. Rev. E* **55**, 1959 (1997).
- [27] K. J. Packer, S. Stapf, J. J. Tessier, and R. A. Damion, *Magn. Reson. Imaging* (to be published).
- [28] E. J. Fordham, S. G. Gibbs, and L. D. Hall, *Magn. Reson. Imaging* **12**, 279 (1994).
- [29] E. O. Stejskal and J. E. Tanner, *J. Chem. Phys.* **42**, 288 (1965).
- [30] A. J. Lucas, S. G. Gibbs, E. W. Jones, M. Peyron, A. D. Derbyshire, and L. D. Hall, *J. Magn. Reson., Ser. A* **104**, 273 (1993).
- [31] IDL Interactive Data Language, Research Systems Inc., Boulder (1995).
- [32] R. Lemaitre and P. M. Adler, *Transp. Porous Media* **5**, 325 (1990).
- [33] S. R. McDougall and K. S. Sorbie, *Petroleum Geosci.* **3**, 161 (1997).
- [34] J. Bear, *Dynamics of Fluids in Porous Media* (Academic, New York, 1975).
- [35] R. Kimmich, S. Stapf, A. I. Maklakov, V. D. Skirda, and E. V. Khozina, *Magn. Reson. Imaging* **14**, 793 (1996).
- [36] L. L. Latour, P. P. Mitra, R. L. Kleinberg, and C. H. Sotak, *J. Magn. Reson., Ser. A* **101**, 342 (1993).
- [37] A. Compte, R. Metzler, and J. Camacho, *Phys. Rev. E* **56**, 1445 (1997).
- [38] N.-W. Han, J. Bhakta, and R. G. Carbonell, *AIChE. J.* **31**, 277 (1985).
- [39] P. M. Adler, *Porous Media. Geometry and Transport* (Butterworth-Heinemann, Stoneham, 1992).
- [40] D. R. F. Harleman and R. R. Rumer, *J. Fluid Mech.* **16**, 385 (1963).
- [41] Y. E. Kutsovsky, L. E. Scriven, H. T. Davis, and B. E. Hammer, *Phys. Fluids* **8**, 863 (1996).
- [42] G. P. Wadsworth and J. G. Bryan, *Introduction to Probability and Random Variables* (McGraw-Hill, New York, 1960).
- [43] S. Stapf and K. J. Packer (unpublished).